Intelligent Methodology for Sensing, Modeling and Control of Pulsed GTAW Part 2 — Butt Joint Welding

Double variable intelligent control incorporated with a fuzzy neural network and expert system is proposed for bead shape control during butt joint welding

BY S. B. CHEN, D. B. ZHAO, L. WU AND Y. J. LOU

ABSTRACT. This paper addresses intelligent techniques for the quality control of the pulsed gas tungsten arc welding process for butt joints, and it is a development to Ref. 1. Because there exist some important differences in butt joint welding and bead-on-plate welding, the modeling and control scheme in Ref. 1 does not completely fit for butt joint welding. In this paper, the differences between the two were investigated. The shape and size parameters for the weld pool were used to describe the weld puol geometry. A new real-time algorithm was developed for the size and shape parameters. A size and shape neural network model (SSNNM) was established to predict the maximum backside width. The model accuracy was verified. Furthermore, a self-learning fuzzy neural network controller (FNNC) was designed for control of the maximum backside width and the fuzzy rules were modified online. Based on the FNNC, and combined with an expert system, a double-input and double-output (DIDO) intelligent controller was developed for controlling the maximum backside width and the shape of the weld pool. Experiment results showed the DIDO intelligent controller could form a better butt joint weld.

Introduction

As is well known, quality control of weld penetration and weld shape is a complicated problem in arc welding. When using the GTAW process on thin-plate mild steel, full joint penetration is an essential factor for ensuring weld quality. Weld bead width, especially backside bead width, is a main factor for evaluating weld quality. In a previous investigation (Ref. 1), the existing sensing and control methods for penetration control were reviewed. Examples of the visual sensing systems reviewed are infrared (Refs. 2, 3), laser-strobe (Refs. 4, 5), laser-structured light (Ref. 6) and coaxial viewing (Refs. 7–9). These sensing systems paved the way for sensing and control of the welding process.

During bead-on-plate welding, the backside width of the weld pool can be predicted and controlled by the heat balance of the weld pool, or the weld pool geometry. Weld shape is ensured by the heat balance between the input and output of the welding process. A nonlinear first-order model was obtained for relating the input welding current to the output weld pool radius. Both the time constant and gain of the first order transfer function have resulted from some simplification (Ref. 10). Because of the plasma impact, the surface of the arc weld pool is depressed. The average depression of the solidified weld was found to have a good linear correlation with the backside bead width. The arc welding process was modeled and an adaptive control system was completed to achieve the desired backside width (Ref.11).

With butt joint welding, the welding parameters are more complex and the correlations among the welding parameters and the geometry of the weld pool become more nonlinear. The weld pool geometry, incorporating size parameters, such as width and length, and shape parameters, such as rear angles, can be used to characterize the shape of the weld pool. Accurate estimation of the backside width can be generated by a neural network model (Ref. 12). Intelligent methodology, such as fuzzy inference, neural network and expert system, is used for modeling and controlling the nonlinear welding process (Refs. 13, 14). A self-learning fuzzy neural control scheme was presented for real-time control of the head width during pulsed GTAW (Ref. 15).

In a previous investigation (Ref. 1), the backside width was predicted and controlled accurately by the topside size parameters during bead-on-plate welding. However, when the same experiments were carried out for butt joint welding, the shape of the weld pool became much more complicated. This shape made it difficult to characterize the backside width using the bead-on-plate welding information. Based on the previous investigation (Ref. 1), the differences between the two welding approaches are reported in this paper. Effective intelligent techniques for an

KEY WORDS

Bead Size
Bead Width
Expert System
Fuzzy Logic
GTAW-P
Intelligent Controller
Neural Networks
Weld Geometry

S. B. CHEN, previously with the Harbin Institute of Technology, Harbin, P.R. China, is now with Shanghai Jiao Tong University, Shanghai, P.R. China. D. B. ZHAO, L. WU and Y. J. LOU are with National Key Laboratory of Advanced Welding Production Technology, Harbin Institute of Technology, Harbin, P.R. China.

image processing algorithm, modeling method and control scheme are proposed for butt joint welding.

Neural Network Model for Welding Butt Joints

Based on the visual sensing method developed in the bead-on-plate welding approach (Ref. 1), butt joint welding experiments were carried out on mild steel. The model relating welding parameters and topside size parameters to backside width was also established from the welding data. Results showed the two size parameters (the maximum width W_{fmax} and the maximum half-length L_{fmax}) varied in a narrow range, while the shape of the weld pool and backside width changed significantly. Thus, the models with the size parameters of the weld pool as the inputs could not accurately predict the backside width. The geometry of the weld pool should be characterized as the size and shape parameters.

Size and Shape Parameters of the Weld Pool

The geometry of the weld pool should be characterized as the size and shape parameters. In this study, the rear width of the weld pool is proposed as the shape parameter, with the definition shown in Fig. 1A. The definition of the backside size parameter is the same as in Ref. 1 and shown in Fig. 1B. The shape parameter is represented by the rear width because the rear shape of the weld pool is sensitive, while the front portion of the weld pool maintains nearly a half circle despite different welding conditions.

In Fig. 1A, the maximum topside width of the weld pool is denoted as W_{fmax}. The center of the maximum width is point a. The topside half-length L_{fmax} is defined as the distance between the rear point b of the weld pool and point a. The rear area of the weld pool S_{fmid} is defined as the area surrounded by the maximum width and the rear boundary. Ten rear widths W_{fi} (i = 1, 2...10) are defined as the shape parameters of the weld pool, shown in Fig. 1A. W_{f10} is also W_{fmax}.

Image Processing for Determining Size and Shape Parameters of the Weld Pool

For determining the size and shape parameters on-line, a new image-processing algorithm was developed based on the previous work. The algorithm consists of the following steps: filter, edge detection, edge recognition, regression of edge points and parameter calculation.

Figure 2A shows the direction definitions of the topside image in the image coordinates. The image is smoothed with the similar method used in bead-on-plate welding (Ref. 1).

The edge of the weld pool causes the most concern. It is characterized by the change of grayness. The grayness changes smoothly along the edge, but rapidly along its normal line. The edge types can be described as step style, slope style and roof style. Different edge calculation templates, such as gradient template, directional template and regression template, are used to determine different edge styles. The directional template was used to determine edge points for consideration in real-time control. The angle between the welding direction (*fkw*) and the axis *y* was 28 deg. The directional template was along the welding direction, and the definition is shown in Fig. 2B. The direction template points 1~9 were calculated by the interpolation algorithm with the surrounding image points printed in circles. To reduce on-line computation, a reference table was established for the interpolation calculation. To eliminate the disturbance from arc center on detecting the edge points, the directional template is selected as

$$h(m,n)=\begin{bmatrix}-20 & -20 & -20\\ 0 & 0 & 0\\ 20 & 20 & 20\end{bmatrix} \quad (1)$$

The complete image processing results are shown in Fig. 3. Figure 3C shows the threshold image after the edge detection with the directional template. The boundary of the weld pool appears distinguishable, and the arc center and other noise points are effectively removed.

The rear point D, the central point C and the maximum width points A and B can be derived by scanning along *fkw* and the vertical welding direction *fkv*. All the edge points can be derived with the same method. However, the edge curve was not smooth and some disturbance points still exist. Two separate four order multinominals were adopted to fit the left and right edges of the weld pool and the

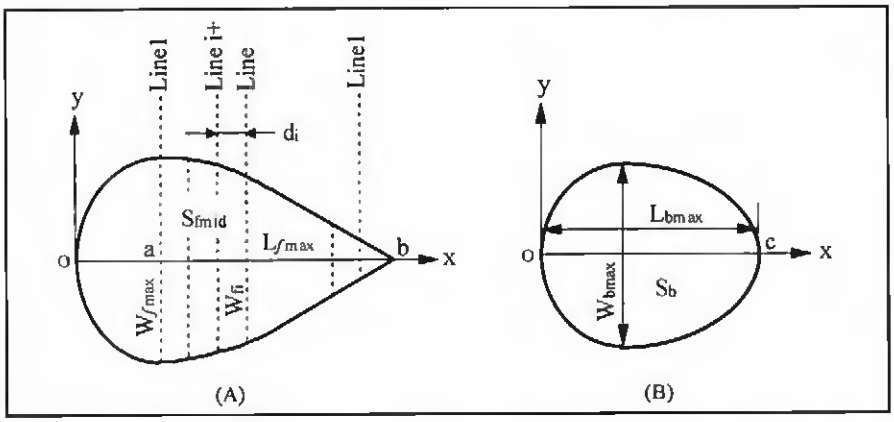

Fig. 1 — Definitions of the topside size and shape parameters of the weld pool. A — Topside; B — backside.

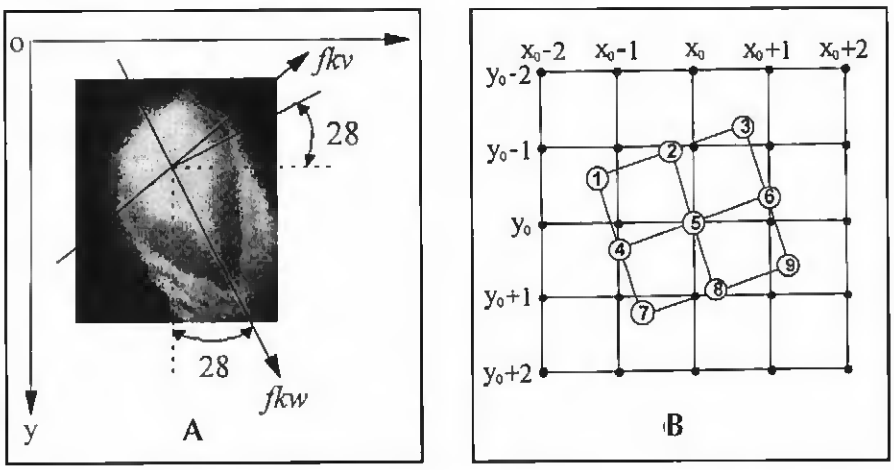

Fig. 2 — Topside image and image processing template. A — The direction definition in the image coordinates; B — the definition of the direction template in the calculating window.

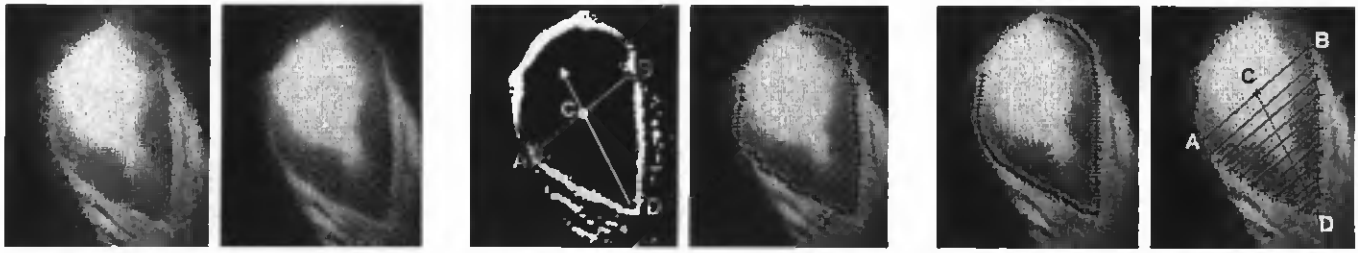

Fig. 3 — Processing of the topside image of the weld pool. A — Original image; B — the smoothed image with EBS; C — the threshold image after edge detection; D — the original edge points; E — the fitted edge points; F — the size and shape parameters.

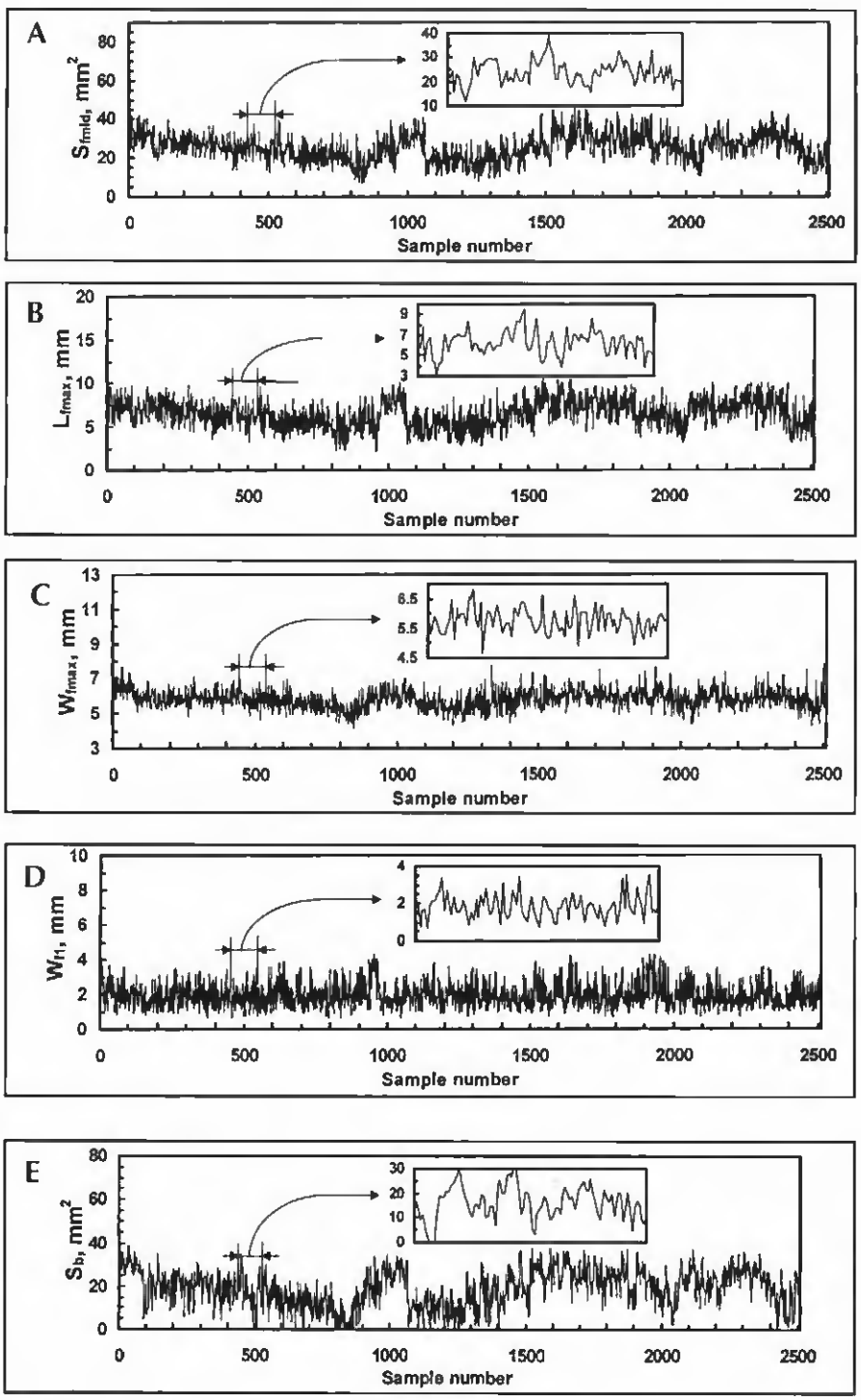

results are shown in Fig. 3E.

Based on the regression result, the size and shape parameters, such as L_{fmax}, W_{fmax}, S_{fmid} and W_{ft}, can be calculated. The backside image-processing algorithm was the same as that for bead-on-plate welding.

The frequency of the pulsed GTAW was 1 Hz and the pulse base time was not less than 350 ms. All the image processing algorithm and control scheme was done during the pulse base time. The double-side image processing algorithm was less than 80 ms, running on a PC486-100 MHz computer. The following control scheme was less than 30 ms, making the selected algorithms adequate for the requirements of real-time control.

Experiments and Results on the Neural Network Model

The heat and force influences on the welding process were determined by the variations of welding parameters such as peak current (I_p), base current (I_b), duty ratio (δ), travel speed (V_w), arc voltage (U_p) and so on. Therefore, different welding parameters were related to differences in weld pool geometry. To establish a valid process model, all kinds of welding conditions should be considered during the experiment design. The major welding parameters, such as I_p, δ, V_w, were taken as the input signals of the model. To incorporate all the characteristics of a dynamic welding process, the inputs were designed with white noise signals because of the widespread spectrum and noncorrelation on time.

Butt joint welding experiments were conducted on a 2-mm-thick mild steel specimen without any surface preparation. A satisfactory weld shape was obtained with the following welding parameters: $I_{p0} = 140$ A, $\delta_0 = 45\%$, $V_{w0} = 2.5$ mm/s. The maximum variations for all the inputs were $\Delta I_p = \pm 25$ A, $\Delta\delta = \pm 20\%$, $\Delta V_w = \pm 0.83$mm/s. The corresponding unit step variations were: $dI_p = \pm 5$ A, $d\delta = \pm 5\%$, $dV_w = \pm 0.167$mm/s. Input welding parameters were generated with the

pseudo-random sequence method, using a total of 2800 numbers. Other welding conditions are tabulated in Table 1.

Welding experiments were conducted with the designed input signals, and the size and shape parameters were determined. Figure 4 shows the curves of double-side, typical-size and shape parameters, all of which varied by a wide range under the designed welding parameters. The maximum of W_{fmax} was approximately 8 mm, the maximum of L_{fmax} was approximately 10 mm and the maximum of S_{fmid} was approximately 45 mm^2. The maximum of W_{bmax} was approximately 7.5 mm, the maximum of L_{bmax} was approximately 9.0 mm and the maximum of S_b was approximately 40.0 mm^2. When partial penetration occurred, the backside size parameters decreased to zero. Therefore, multiple welding states were activated and the experimental data could he thought as covering all the penetration situations. The experimental curves also showed that each group of topside size and shape parameters, and backside size parameters, varied in a similar manner.

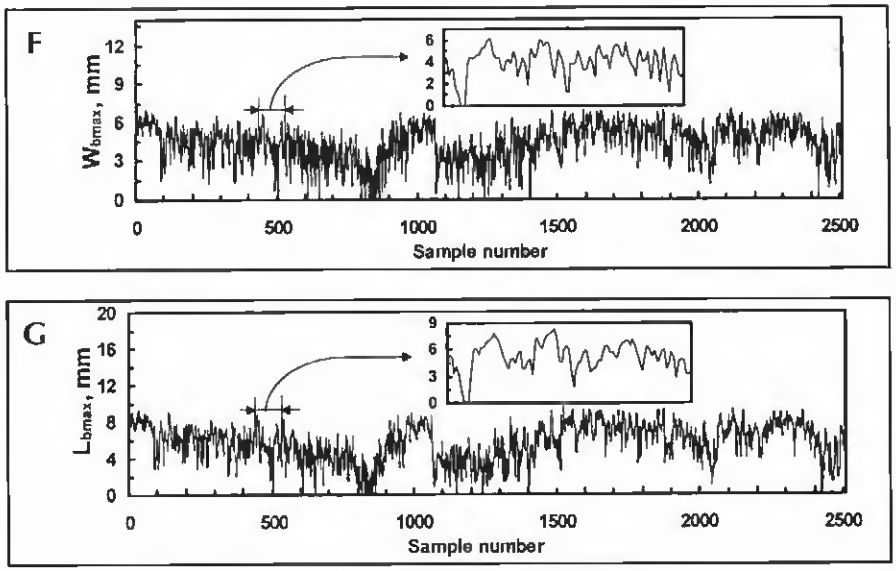

Fig. 4 — The typical double-side size and shape parameters of the weld pool. A — S_{fmid}; B — L_{fmax}; C — W_{fmax}; D — W_{fi}; E — S_b; F — W_{bmax}; G — L_{bmax}.

Table 1 — Experimental Conditions of Pulsed GTAW

Welding Conditions	Pulse Frequency	Base Current	Electrode Diameter	Angle of Tip	Arc Length	Flow of Ar
Unit	f (Hz)	Ib (A)	ϕ (mm)	θ (deg)	l (mm)	L (L/min)
Value	1	60	3.2	30	3.5	8.0

The Neural Network Modeling Architecture

As is well known, neural networks are suitable for modeling a nonlinear process. A size and shape neural network model (SSNNM) for a dynamic welding process was established to relate the welding parameters, and the topside size and shape parameters, to the backside size parameters. To establish a dynamic process model, the input variables of the SSNNM included the welding parameters, the topside size and shape parameters and their last two history values, a total of 48 numbers. The number of elements in the hidden layer was 30. The output variable of the model was each of the backside size parameters (W_{bmax}, L_{bmax} and S_b), so three models for the process were established. The model structure is shown in Fig. 5. At the same time, a single-size neural network model (SNNM) with the welding parameters and the topside size parameters as the inputs was established for comparison.

Based on the test data, the three models for W_{bmax}, L_{bmax} and S_b were trained. The training was performed using the commercial neural network software, Professional II plus. Sigmoid function was selected as the nonlinear function of the neuron. Delta-bar-delta (DBD) was selected as the learning algorithm. The learning coefficients and momentum ratio were automatically determined by the algorithm for each 5000 training cycles. The total training cycle was 20,000.

Simulation tests were carried out with the models SSNNM and SNNM. The error statistic results between the outputs of the models and the test data are tabulated in Table 2. The results indicate the SSNNM can predict the backside size parameters more accurately than the SNNM.

Characteristic Comparison between Bead-on-Plate and Butt Joint Welding

Simulation and experimental results showed the following:

1) The geometry parameters of the weld pool during butt joint welding become more complex than that during bead-on-plate welding. There are some similar geometry parameters, as well as some very different parameters. Therefore, more information on weld pool geometry should supplement the estimating of backside width during butt joint welding.

2) When the pulse peak current and the pulse duty ratio are great and the travel speed is small, the double-side length-to-width ratios in butt joint welding become smaller than that in bead-on-plate welding. When the travel speed increases, the geometry parameters in the length direction become great, while the geometry parameters in the width direction do not change a lot. This phenomenon is not found during head-on-plate welding.

3) The causes for the variations in the geometry parameters may include an irregular root opening and the arc force acting on the weld pool surface. For example, the root opening may play a significant role in determining the depression of the weld pool.

4) The above analysis concludes that the backside width cannot be accurately predicted by the size parameters. The shape parameters should be considered as the model inputs to predict the backside width.

Single-Variable, Self-Learning Fuzzy Neural Network Control

Fuzzy Control Rules Determined from the Experiment Data

Fuzzy control rules express the fuzzy relationship between the inputs and the outputs of the control system. To achieve the fuzzy control rules for pulsed gas tungsten arc welding of a butt joint, a C-mean dynamic polymerizing algorithm was used to determine the fuzzy rules

Table 2 — The Comparison between SNNM and SSNNM Statistic Results

	Backside Maximum Width $W_{b\max}$			Backside Maximum Length $L_{b\max}$			Backside Area S_b		
	Maximum Error (mm)	Average Error (mm)	Root-Mean-Square Error (mm)	Maximum Error (mm)	Average Error (mm)	Root-Mean-Square Error (mm)	Maximum Error (mm²)	Average Error (mm²)	Root-Mean-Square Error (mm²)
SNNM	2.95	0.44	0.57	3.46	0.54	0.71	9.40	3.48	3.04
SSNNM	1.54	0.15	0.19	1.38	0.16	0.21	4.03	0.59	0.72

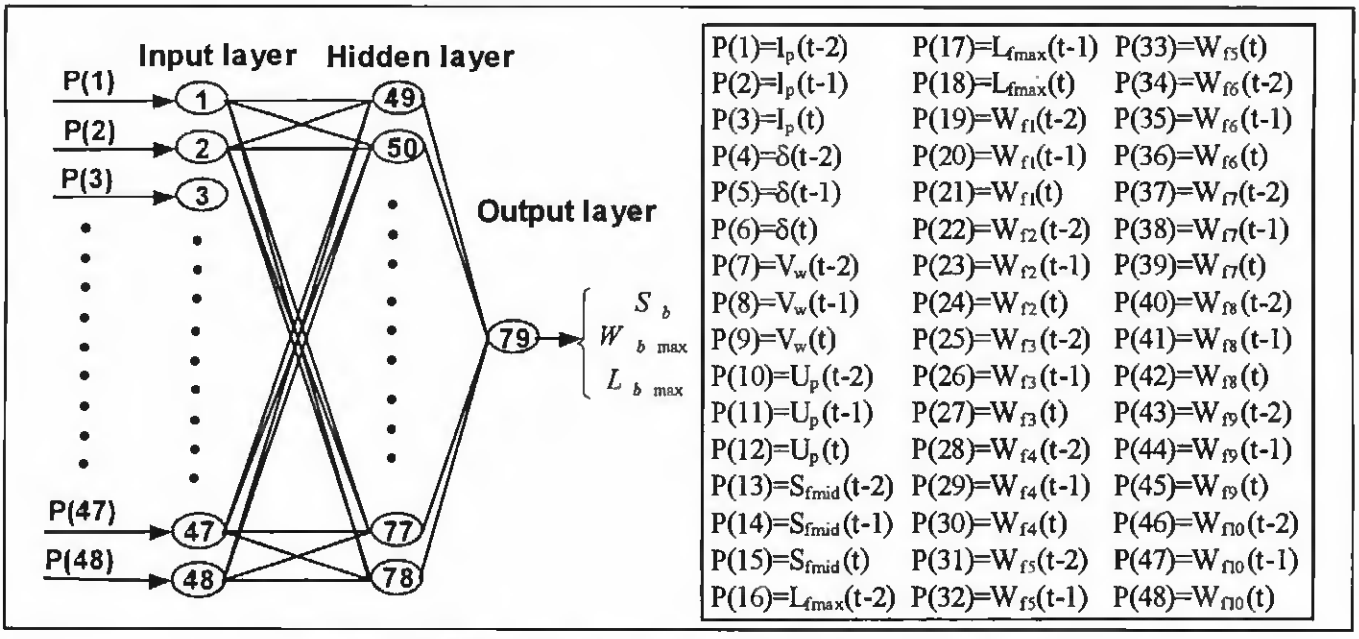

P(1)=l_p(t-2)	P(17)=L_{fmax}(t-1)	P(33)=W_{f5}(t)
P(2)=l_p(t-1)	P(18)=L_{fmax}(t)	P(34)=W_{f6}(t-2)
P(3)=l_p(t)	P(19)=W_{f1}(t-2)	P(35)=W_{f6}(t-1)
P(4)=δ(t-2)	P(20)=W_{f1}(t-1)	P(36)=W_{f6}(t)
P(5)=δ(t-1)	P(21)=W_{f1}(t)	P(37)=W_{f7}(t-2)
P(6)=δ(t)	P(22)=W_{f2}(t-2)	P(38)=W_{f7}(t-1)
P(7)=V_w(t-2)	P(23)=W_{f2}(t-1)	P(39)=W_{f7}(t)
P(8)=V_w(t-1)	P(24)=W_{f2}(t)	P(40)=W_{f8}(t-2)
P(9)=V_w(t)	P(25)=W_{f3}(t-2)	P(41)=W_{f8}(t-1)
P(10)=U_p(t-2)	P(26)=W_{f3}(t-1)	P(42)=W_{f8}(t)
P(11)=U_p(t-1)	P(27)=W_{f3}(t)	P(43)=W_{f9}(t-2)
P(12)=U_p(t)	P(28)=W_{f4}(t-2)	P(44)=W_{f9}(t-1)
P(13)=S_{fmid}(t-2)	P(29)=W_{f4}(t-1)	P(45)=W_{f9}(t)
P(14)=S_{fmid}(t-1)	P(30)=W_{f4}(t)	P(46)=W_{f10}(t-2)
P(15)=S_{fmid}(t)	P(31)=W_{f5}(t-2)	P(47)=W_{f10}(t-1)
P(16)=L_{fmax}(t-2)	P(32)=W_{f5}(t-1)	P(48)=W_{f10}(t)

Fig. 5 — The structure of the size and shape neural network model (SSNNM).

from the welding experiment data. As a result of actual arc welding, the maximum backside width W_{bmax} was defined as the controlled variable and the pulse duty ratio δ of the welding current was the control variable. To identify the dynamic characteristic of pulsed gas tungsten arc welding of a butt joint, experiments were undertaken using a pseudo-random sequence of δ as the input of the actual welding system, and 2109 normalizing sample data pairs {δ, W_{bmax}} were achieved.

The error E of W_{bmax} and the change in error CE were chosen as the input fuzzy variables of the fuzzy control system, and δ was chosen as the output fuzzy variable, described as U of the fuzzy control system. The fuzzy subsets of these fuzzy linguistic variables can be described as {*NB, NM, NS, ZO, PS, PM, PB*}, where *N, ZO* and *P* mean negative, zero and positive, and *B, M* and *S* mean big, medium and small.

To determine the fuzzy control rules of the pulsed gas tungsten arc welding process, the C-mean dynamic polymerizing algorithm is described as follows:

Step 1. The initial centers of each fuzzy subset of E and CE are chosen as shown in Table 3. We define the polymerizing center of i^{th} fuzzy subset of E as $ZE_i(l)$, the polymerizing center of j^{th} fuzzy subset of CE as $ZCE_j(l)$ and l means iterating number of the algorithm, with a rise from 1.

Step 2. The Euclidean distance between a sample data pair and a polymerizing center of the fuzzy subset is

$$D\left(e_k, ZE_i(l), ce_k, ZCE_j(l)\right) = \sqrt{\left(e_k - ZE_i(l)\right)^2 + \left(ce_k - ZCE_j(l)\right)^2} \quad (2)$$

where e_k denotes k^{th} sample value of E, and ce_k denotes k^{th} sample value of CE. Calculating the Euclidean distance between each sample data pair and each polymerizing center of the fuzzy subset of E and CE, if

$$D\left(e_k, ZE_i(l), ce_k, ZCE_m(l)\right) = \min_{\substack{i=1,\ldots,7 \\ j=1,\ldots,7}} \left\{D\left(e_k, ZE_i(l), ce_k, ZCE_j(l)\right)\right\} \quad (3)$$

Then e_k belongs to ZE_i, and c_{ek} belongs to ZCE_m.

Step 3. $l = l + 1$, calculating new polymerizing center of the fuzzy subset of E and CE as follows:

$$ZE_i(l) = \frac{1}{n_i}\sum_{k=1}^{n_i} e_k^i \quad i = 1,2,\ldots,7 \quad (4)$$

$$ZCE_j(l) = \frac{1}{n_j}\sum_{k=1}^{n_j} ce_k^j \quad j = 1,2,\ldots,7 \quad (5)$$

Where n_i is the sample number of the i^{th} fuzzy subset of E, n_j is the sample number of the j^{th} fuzzy subset of CE, $e^i{}_k$ is the k^{th} sample of the i^{th} fuzzy subset of E, and cei_k is the k^{th} sample of the j^{th} fuzzy subset of CE.

Step 4. Calculating the sum of square-error $J_c(l)$ as follows:

$$J_c(l) = \sum_{i=1}^{7}\sum_{k=1}^{n_i}\left(e_k^i - ZE_i(l)\right)^2 + \sum_{j=1}^{7}\sum_{k=1}^{n_j}\left(ce_k^j - ZCE_j(l)\right)^2 \quad (6)$$

Step 5. If $|J_c(l) - J_c(l-1)| \le \varepsilon$, where ε denotes the preset polymerizing precision, and if the polymerizing results converge, the algorithm stops, otherwise, return to Step 2, and the algorithm continues.

Using the above C-mean dynamic polymerizing algorithm, the final polymerizing centers of the fuzzy subsets of E and CE were derived, as shown in Table 4. We defined the centers of the fuzzy subset of the output fuzzy variable U as {–0.87, –0.58, –0.29, 0.00, +0.29, +0.58,

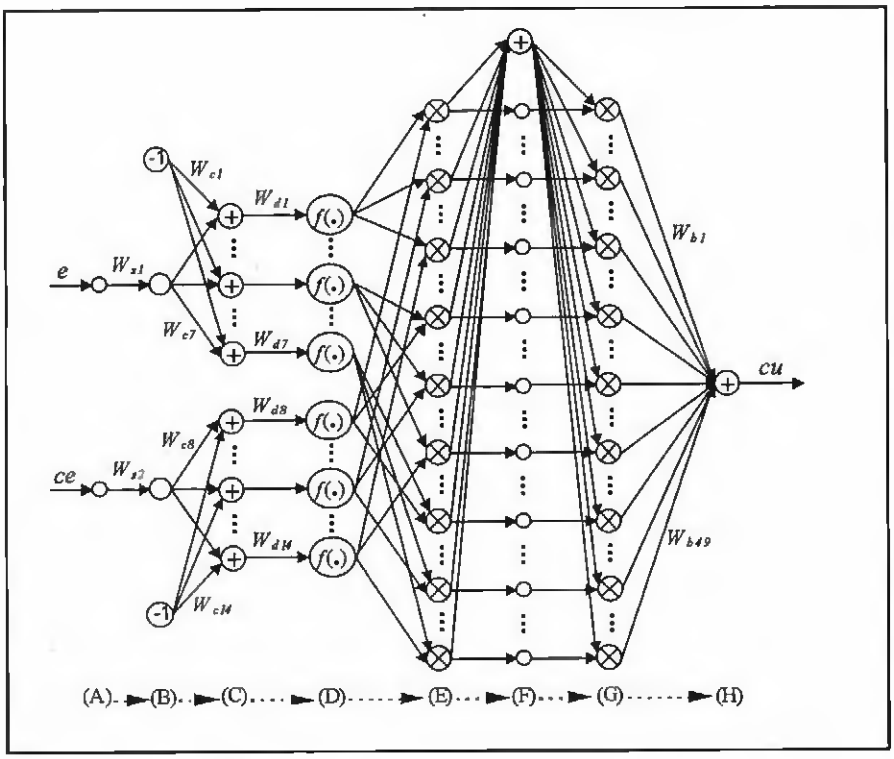

Fig. 6 — The structure of the fuzzy neural network controller (FNNC).

Table 3 — The Initial Polymerizing Centers

	NB	NM	NS	ZO	PS	PM	PB
E	–0.95	–0.75	–0.15	0.00	0.25	0.65	0.85
CE	–0.80	–0.60	–0.25	0.00	0.30	0.60	0.90

Table 4 — The Final Polymerizing Centers

	NB	NM	NS	ZO	PS	PM	PB
E	–0.80	–0.54	–0.29	–0.03	0.21	0.50	0.80
CE	–0.85	–0.58	–0.32	0.04	0.30	0.55	0.82

Table 5 — The Fuzzy Control Rules for Pulsed Gas Tungsten Arc Butt Joint Welding

U / E \ CE	NB	NM	NS	ZO	PS	PM	PB
NB	PB	PB	PB	PM	PS	ZO	ZO
NM	PB	PB	PM	PM	PS	ZO	ZO
NS	PB	PM	PM	PS	ZO	NS	NS
ZO	PM	PM	PS	ZO	NS	NM	NM
PS	PS	PS	ZO	NS	NM	NM	NB
PM	ZO	ZO	NS	NM	NM	NB	NB
PB	ZO	ZO	NS	NM	NB	NB	NB

+0.87). On the basis of the polymerizing results of *E* and *CE*, the fuzzy control rules for welding a butt joint were obtained by the principle of the nearest distance, as tabulated in Table 5.

Based on the analysis of the welding process for a butt joint, using fuzzy inference technology and artificial neural network methodology, a self-learning fuzzy neural network controller for welding a butt joint is presented.

Fuzzy Neural Network Controller (FNNC)

Each layer and each node of the fuzzy neural network is related to a part of the fuzzy system. According to the membership function and inference process, all the nodes and weights have certain physical meanings. The j^{th} fuzzy control rule of the fuzzy control system is denoted as

Rule j: IF (E is Ei) and (CE is CEi)
THEN (CU is CUi), j = 1,2,···m (7)

Where Ei ∈ {E_1,E_2,···E_7}, CEi ∈ {CE_1, CE_2, ···CE_7}, CUi ∈ {CU_1, CU_2, ···CU_7}.

The output of the fuzzy system can be calculated as

$$cu = \frac{\oplus_{j=1}^{m} h_j CU^j}{\oplus_{j=1}^{m} h_j} \qquad (8)$$

where *cu* is the crisp value of the output variable of the control system, ⊕ means algebraic sum and h_j is the matched degree between the current input and the j^{th} fuzzy control rule, described as

$$h_j = \mu_E{}^j(e) \cdot \mu_{CE}{}^j(ce) \qquad (9)$$

where $\mu_E{}^j(e)$ is the membership of e belonging to the fuzzy subset E^j, and $\mu_{CE}{}^j(e)$ is the membership of *ce* belonging to the fuzzy subset CE^j.

The structure of the fuzzy system can be expressed by a forward neural network. The whole system is denoted as the fuzzy neural network controller (FNNC), shown in Fig. 6, in which the unmarked weights are one. The network includes eight layers, where A~D layers transform the input crisp value to the membership of the fuzzy subsets of *E* and *CE*, where *E~F* layers carry out fuzzy inference, *G* layer fulfills fuzzy synthesis, *H* layer acts as fuzzy judging, from which then the crisp output value is acquired.

Supposing the input of the j^{th} node of the l^{th} layer of the FNNC is I^l_j, the output is O^l_j, then the relationship between the input and the output of each layer of the FNNC is described as

A layer: $I^a_j = x_j, O^a_j = I^a_j$,
j= 1,2, $x_1 = e$, $x_2 = ce$ (10)

B layer: $I^b_j = W_{sj} \cdot O^a_i$,
$O^b_j = I^b_j$, j = 1,2 (11)

C layer: $I^c_k = (O^b_i - W_{ck})$, $O^c_k = I^c_k$,
j = [(k–1)/7] + 1, k = 1,2 ···14 (12)

D layer: $I^d_i = O^c_i \cdot W_{di}$,
$O^d_i = e^{-(I^d_i)^2}$, i = 1,2,...14 (13)

E layer: $I^e_k = O^d_i \cdot O^d_j$, $O^e_k = I^e_k$, i = 1,2···,7, j = 8,9···14,
k = 7i +j – 14 (14)

F layer: $I^f_1 = \oplus^{49}_{k=1} O^e_k$,
$O^f_1 = (1/I^f_1)$, $I^f_k = O^e_{k-1}$,
$O^f_k = I^f_k$, k = 2,3···,50 (15)

G layer: $I^g_k = O^f_1 \cdot O^f_{k+1}$,
$O^g_k = I^g_k$, k = 1,2,···,49 (16)

H layer: $I^h_1 = \oplus^{49}_{k=1} O^g_k \cdot W_{bk}$,
$O^h_1 = I^h_1$ (17)

Learning Algorithm of the Fuzzy Neural Network Controller

The learning process of the FNNC consists of off-line and on-line learning. The off-line learning of the FNNC is to get the initial membership of the fuzzy subsets of input fuzzy variables *E* and *CE*, determine the initial weights between the nodes in the G~H layer and reduce the on-line learning time of the FNNC. The

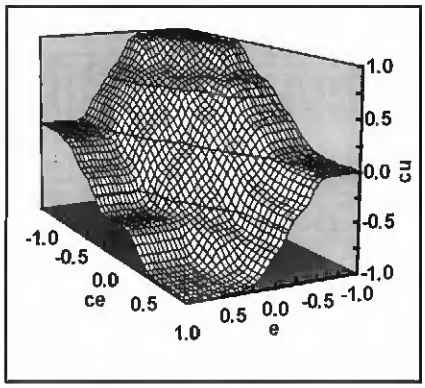

Fig. 7 — The initial relationship surface between the inputs and outputs of the FNNC.

on-line learning of the FNNC is to modify the membership of the fuzzy subsets and fuzzy control rules during butt joint welding, so that the FNNC can adapt to the varying conditions.

The learning sample of the FNNC is provided with the fuzzy control rules, shown in Table 5. The initial quantification factor W_{si} of E and CE is 6. The initial center W_{ci} of the membership function of the fuzzy subsets in E is {–4.80, –3.24, –1.72, 0.00, 1.24, 3.00, 4.80}. The initial distributing parameters W_{di} of the membership function of the fuzzy subsets in E is {1.068, 1.082, 1.029, 1.126, 1.111, 0.936, 0.926}. The initial centers W_{ci} of the membership function of the fuzzy subsets in CE are {–5.07, –3.45, –1.90, 0.00, 1.79, 3.28, 4.93}, and initial distributing parameters W_{di} of the membership function of the fuzzy subsets in CE is {1.029, 1.052, 0.966, 0.903, 1.016, 1.062, 1.010}. The initial value of the weights W_{bi} can be acquired by the off-line learning of the FNNC. By training the FNNC for 500 times using a hack-propagation algorithm, the initial membership of the fuzzy subsets of E and CE were obtained. The relationship surface between the input and output of the FNNC after off-line learning is shown in Fig. 7.

The goal of the on-line learning of the FNNC is to minimize the output error of the controlled object. The error function is defined as

$$E^* = \frac{1}{2}\sum_{i=1}^{n}(y_i - y_d)^2 \tag{18}$$

where n is the number of the learning sample, y_i denotes the output of the controlled object and y_d denotes the desired output of the controlled object.

The weights of the FNNC are adjusted hy error back-propagation learning algorithms. The formulations are shown as

H layer:

$$\delta_k^h = -\frac{\partial E^*}{\partial I_k^h} = \sum_{i=1}^{n}(y_i - y_d) \cdot \frac{\partial y_i}{\partial u} \cdot f'\left(I_k^h\right),\ f'\left(I_k^h\right) = \frac{\partial O_1^h}{\partial I_k^h} = 1,\ k = 1,2,\cdots,49 \tag{19}$$

$$W_{bk}(t+1) = W_{bk}(t) + \eta \cdot \delta_k^h \cdot O_k^g + \alpha \cdot \left[W_{bk}(t) - W_{bk}(t-1)\right] \tag{20}$$

G layer:

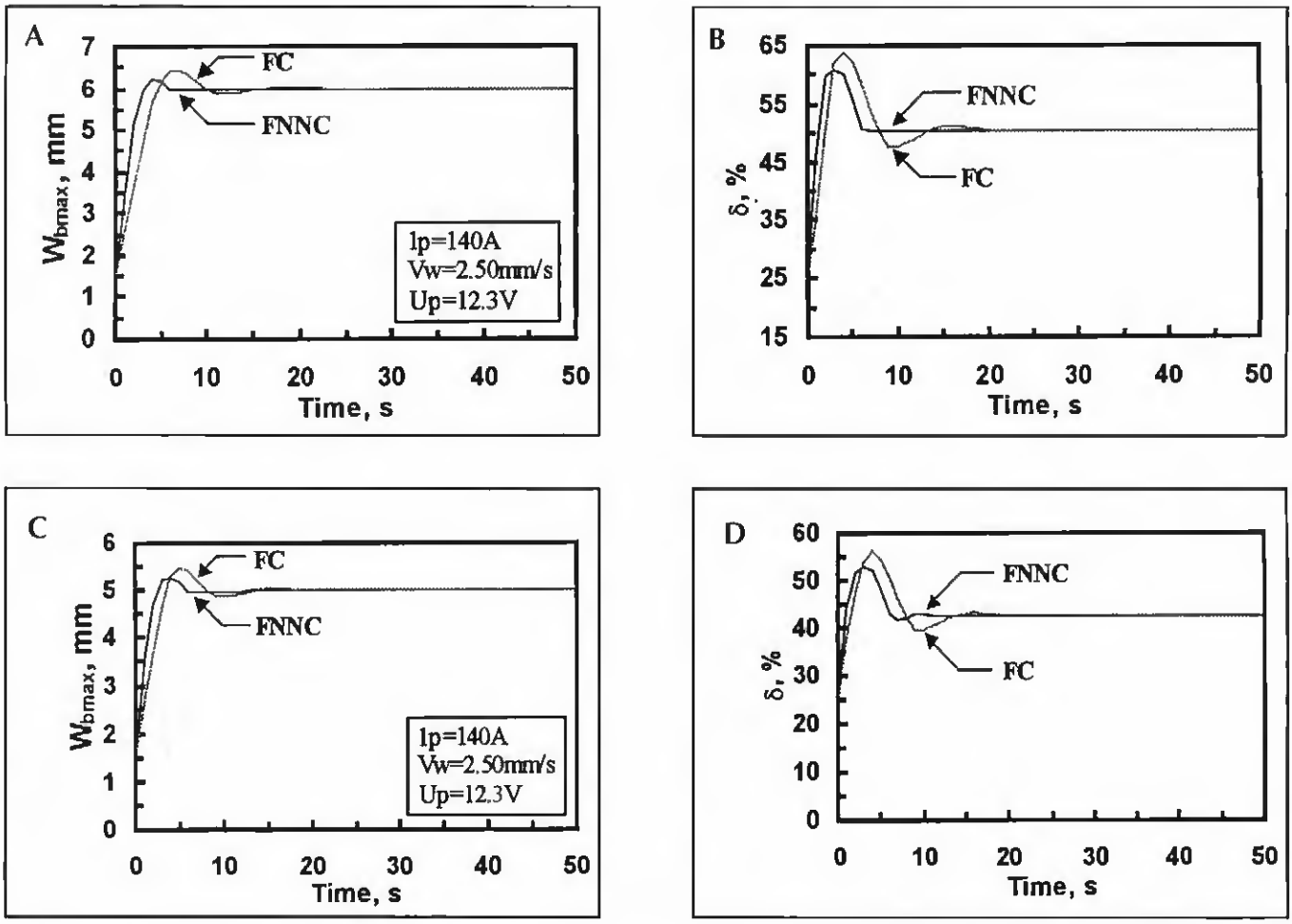

Fig. 8 — Simulation curves of the FNNC. A — W_{bmax} with W_{mbmax} = 6 mm; B — d with W_{mbmax} = 6 mm; C — W_{bmax} with W_{mbmax} = 5 mm; D — d with W_{mbmax} = 5 mm.

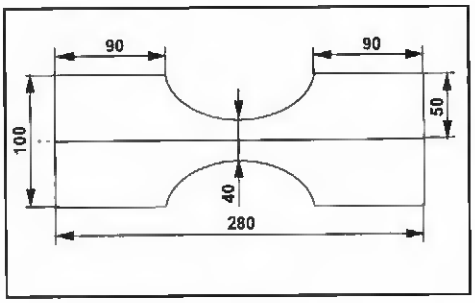

Fig. 9 — Geometry of the dumbbell-shaped workpiece.

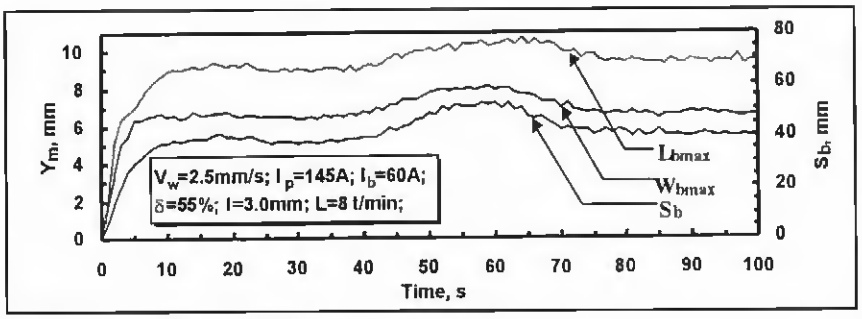

Fig. 10 — Weld pool sizes for the dumbbell-shaped workpiece using constant welding parameters.

$$\delta_k^g = -\frac{\partial E^*}{\partial I_k^g} = \delta_k^h \cdot W_{bk}(t) \cdot f'\left(I_k^g\right),$$

$$f'\left(I_k^g\right) = \frac{\partial O_k^g}{\partial I_k^g} = 1,\ k = 1, 2, \cdots, 49 \tag{21}$$

F layer:

$$\delta_1^f = -\frac{\partial E^*}{\partial I_1^f} = \sum_{l=1}^{49}\left(\delta_l^g \cdot O_{l+1}^f\right) \cdot f'\left(I_1^f\right),\ f'\left(I_1^f\right) = \frac{\partial O_1^f}{\partial I_1^f} = -\left(O_1^f\right)^2 \tag{22}$$

$$\delta_k^f = -\frac{\partial E^*}{\partial I_k^f} = \delta_l^g \cdot O_1^f \cdot f'\left(I_k^f\right),\ f'\left(I_k^f\right) = \frac{\partial O_k^f}{\partial I_k^f} = 1,$$

$$l = k - 1,\ k = 2, 3, \cdots, 50 \tag{23}$$

E layer:

$$\delta_k^e = -\frac{\partial E^*}{\partial I_k^e} = \left(\delta_1^f + \delta_l^f\right) \cdot f'\left(I_k^e\right),\ f'\left(I_k^e\right) = \frac{\partial O_k^e}{\partial I_k^e} = 1,$$

$$l = k + 1,\ k = 1, 2, \cdots, 49 \tag{24}$$

D layer:

$$\delta_k^d = -\frac{\partial E^*}{\partial I_k^d} = \sum_{l=1}^{7}\left(\delta_{7(k-1)+l}^e \cdot O_{l+7}^d\right) \cdot f'\left(I_k^d\right),\ f'\left(I_k^d\right) = \frac{\partial O_k^d}{\partial I_k^d} = -2I_k^d \cdot O_k^d,\ k = 1, \cdots, 7 \tag{25}$$

$$\delta_k^d = -\frac{\partial E^*}{\partial I_k^d} = \sum_{l=1}^{7}\left(\delta_{7(l-1)+k-7}^e \cdot O_l^d\right) \cdot f'\left(I_k^d\right),\ f'\left(I_k^d\right) = \frac{\partial O_k^d}{\partial I_k^d} = -2I_k^d \cdot O_k^d,\ k = 8, \cdots, 14 \tag{26}$$

$$W_{dk}(t+1) = W_{dk}(t) + \eta \cdot \delta_k^d \cdot O_k^c + \alpha \cdot \begin{bmatrix} W_{dk}(t) \\ -W_{dk}(t-1) \end{bmatrix},\ k = 1, 2 \cdots 14 \tag{27}$$

C layer:

$$\delta_k^c = -\frac{\partial E^*}{\partial I_k^c} = \delta_k^d \cdot W_{dk}(t) \cdot f'\left(I_k^c\right),\ f'\left(I_k^c\right) = \frac{\partial O_k^c}{\partial I_k^c} = 1,\ k = 1, 2 \cdots, 14 \tag{28}$$

$$W_{ck}(t+1) = W_{ck}(t) + \eta \cdot \delta_k^c \cdot O_k^b + \alpha \cdot \left[W_{ck}(t) - W_{ck}(t-1)\right] \tag{29}$$

B layer:

$$\delta_k^b = -\frac{\partial E^*}{\partial I_k^b} = \sum_{l=1}^{7} \delta_{7(k-1)+l}^c \cdot f'\left(I_k^b\right),\ f'\left(I_k^b\right) = \frac{\partial O_k^b}{\partial I_k^b} = 1,\ k = 1, 2 \tag{30}$$

$$W_{sk}(t+1) = W_{sk}(t) + \eta \cdot \delta_k^b \cdot O_k^a + \alpha \cdot \left[W_{sk}(t) - W_{sk}(t-1)\right] \tag{31}$$

where δ_l^j denotes the back propagating error of the j^{th} node in the l^{th} layer of the FNNC, η is the learning coefficient and α is the momentum factor. The regulation of the FNNC weights can be realized with Equations 19–31, which make up a one-step learning algorithm of the FNNC.

Simulation of the Fuzzy Neural Network Controller

Given the maximum backside width W_{mbmax} of 5.0 and 6.0 mm, the FNNC simulations for butt joint welding were accomplished. The learning coefficient η was 0.45 and the momentum factor α was 0.20. We defined the error *e* as ∈[–2.0 mm, +2.0 mm], the change in error *ce* as ∈[–1.5 mm, +1.5 mm] and the change in the pulse duty ratio *cu* as ∈[–12%, +12%].

Given W_{mbmax} as 6.0, the simulation results are shown in Fig. 8A, B. The overshoot of W_{bmax} was 3.26%, the regulating time was 3 s and δ stabilized at 51%. The simulation results of W_{mbmax} = 5.0 are shown in Fig. 8C, D. The overshoot of W_{bmax} was 4.51%, the regulating time was 2 s and δ stabilized at 43%. All the simulation results showed the overshoot was small and the regulating time was fast, indicating the FNNC can adapt to the variations in butt joint welding.

Control Experiments by the Fuzzy Neural Network Controller

To investigate the practical use of the FNNC, experiments were conducted with pulsed gas tungsten arc welding of a butt joint. The specimen for the test was mild steel plate of 2-mm thickness, shown in Fig. 9. The dumbbell-shaped specimen imitated the gradual changes in heat-transfer or heat-sink conditions during welding. Figure 10 shows the variations of the backside size parameters, as well as the stable welding parameters. The backside size fluctuated greatly with the different sizes of specimens. The transitions of the weld pool size were distinguished at 35 and 70 pulses.

The FNNC closed-loop control experiments were performed on specimens with a W_{mbmax} of 6.0 mm. The schematic of the control system is shown as Fig. 11. The output variable was δ and the mini-

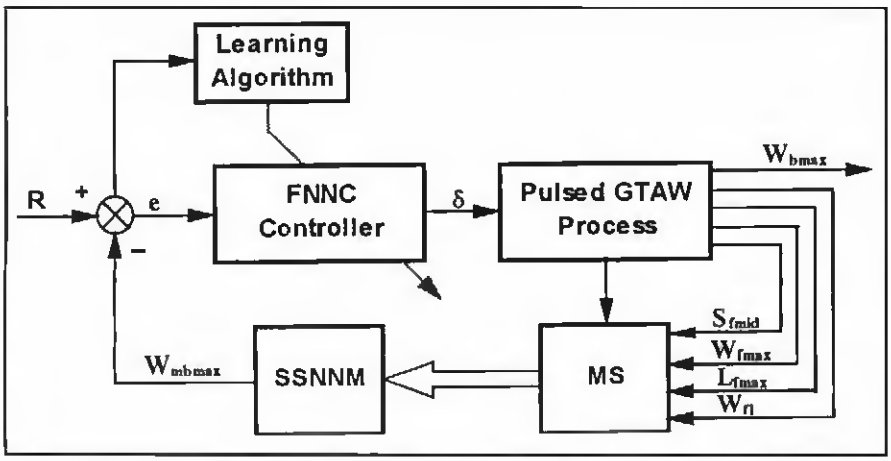

Fig. 11 — Schematic of the FNNC closed-loop control system for pulsed gas tungsten arc welding of a butt joint.

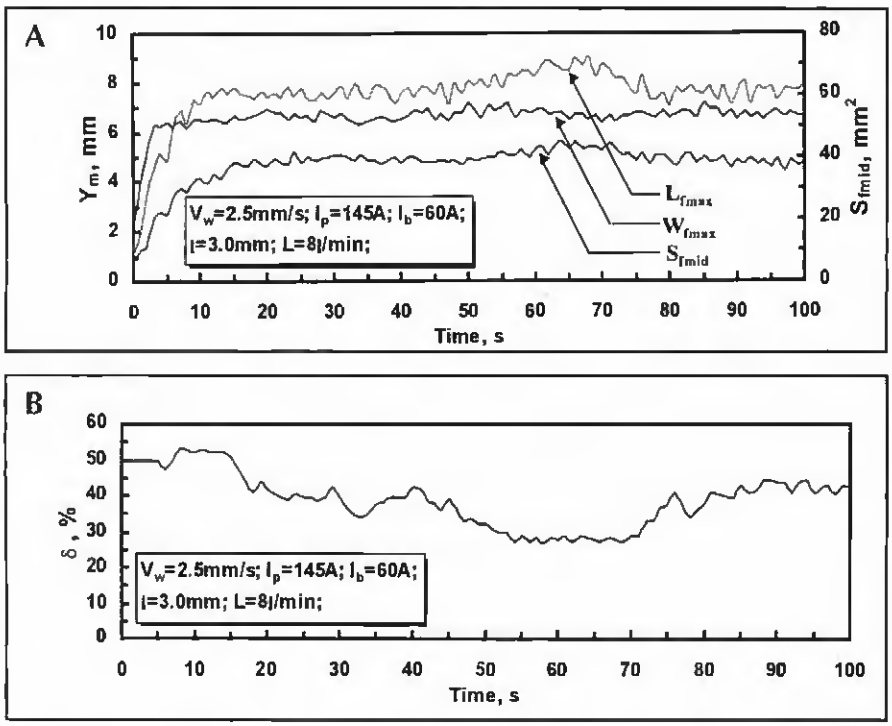

Fig. 12 — FNNC closed-loop control curves of the dumbbell-shape workpiece. A — Backside sizes of the weld pool; B — pulse duty ratio.

mum regulating unit of δ was 1%. W_{bmax} was the control variable. *MS* sensed the topside size and shape parameters, such as W_{fmax}, L_{fmax}, S_{fmid}, the rear widths W_{fi} and the welding parameters. The weights of the network were modified based on the above algorithm for self-learning online. Figure 12 A shows the variations in the backside size parameters, and Fig.12B shows the regulation curve of δ with the variation in heat transfer. The shape of the curve is similar to a skilled operator's manipulation, which verifies a capacity for self-learning. With the W_{bmax} maintained at a given value on the whole, the statistical results showed the maximum error was 0.46 mm, the average error was 0.07 mm and the root-mean-square error was 0.2 mm. This indicates that the size parameters in the width direction can be controlled.

Figure 13 shows the final relationship between input and output of the FNNC, which contains the fuzzy control rules. The differences between the initial and final surface relationship indicated the surface control rules were modified automatically during welding, and the intelligent control function was realized. The surface relation changed more intensely than the initial relation surface (Fig. 7), which indicated a nonlinear function existed in the butt joint welding.

Double Variables in Intelligent Control

The backside maximum width of the weld pool can be controlled by the single variable controller, but the backside weld may not always be satisf
actory. Through these investigations, the topside half-length and area were found to increase when the backside weld was unsatisfactory. This indicated the regulation of the single pulse duty ratio did not guarantee good weld geometry. Moreover, the step impulse showed the travel speed had an important role with the size parameters in the welding direction. Therefore, the effect from travel speed adjustment should be considered.

Design of the Double-Input and Double-Output Intelligent Controller

An expert system for weld geometry control was applied to adjust welding speed. The double-input and double-output intelligent control system consisted of an expert system and a single-variable fuzzy neural network control.

To some extent, the expert system translates the expert experiences of solving some problems into the generated rules represented by the knowledge base. Basically, an expert system consists of a knowledge hase and a ratiocination machine. The knowledge base provides the expert knowledge in problem regions, and the ratiocination machine yields the control strategy from the knowledge hase according to the current status. The generated rule is often represented as, "If A then B."

The schematic diagram of the closed-loop control system is shown in Fig. 14, where the top dashed-line frame represents the fuzzy neural network for controlling the backside width hy adjusting the pulse duty ratio and the underside dashed-line frame represents the expert system to adjust the travel speed. The inputs of the expert system are L_{fmax} and S_{fmid}, which are combined and transferred to a shape factor γ through the signal converter. The error between γ and the given value γ_g matches the generated rules in the knowledge base of the expert system, yielding the travel speed V_w. V_w with δ are regulating variables of the welding process for fulfilling the control.

When the weld shape is perfect, the

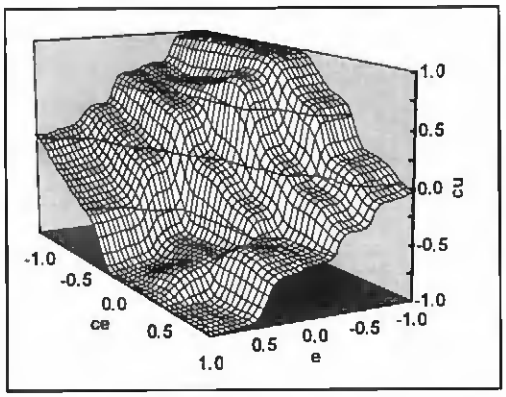

Fig. 13 — The final relationship surfaces between the inputs and outputs of the FNNC.

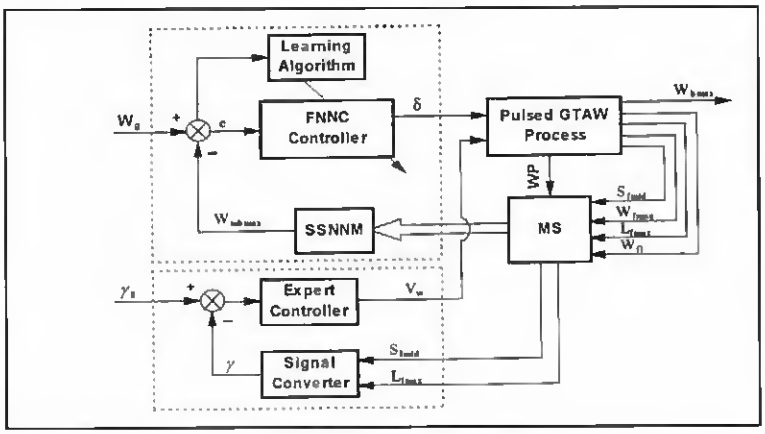

Fig. 14 — Schematic of the closed-loop double-input and double-output intelligent control system for pulsed gas tungsten arc welding of a butt joint.

geometry parameters can be derived from the welding experiment curves. For example, the L_{lmax} is approximately 7.40 mm, and the S_{lmid} is approximately 37.5 mm^2. While the weld shape is not satisfied, L_{lmax} increases to 8.95 mm and S_{lmid} increases to 45.0 mm^2. Based on the above experiences, the input ranges of the expert controller are defined with L_{lmax} = [6.40 mm, 8.40 mm] and S_{lmid} = [30.0 mm^2, 45.0 mm^2]. The center values are 7.40 mm and 37.5 mm^2, respectively. To avoid the effect from the different units and ranges, normalization of the values as shown below is necessary.

$$\bar{x}_L = \frac{x_L - x_{L\,min}}{x_{L\,max} - x_{L\,min}} \qquad (32)$$

$$\bar{x}_S = \frac{x_S - x_{S\,min}}{x_{S\,max} - x_{S\,min}} \qquad (33)$$

where $\bar{x}_L$ and $\bar{x}_S$ are the normalization results. The shape factor γ is determined by the two factors, and defined as

$$\gamma = 0.5\bar{x}_L + 0.5\bar{x}_S \qquad (34)$$

The generated rules of the expert controller are the summarized experiences of specialists and skilled operators. The rules represent human behavior for adjusting travel speed to ensure weld shape. The generated rules for butt joint welding are as follows:

R1: IF γ<0.00 THEN ΔV_w = –0.50 mm/s

R2: IF 0.00 ≤γ<0.20 THEN ΔV_w = –0.33 mm/s

R3: IF 0.20 ≤γ<0.45 THEN ΔV_w = –0.17 mm/s

R4: IF 0.45 ≤γ<0.55 THEN ΔV_w = 0.00 mm/s

R5: IF 0.55≤γ<0.80 THEN ΔV_w = 0.17 mm/s

R6: IF 0.80 ≤γ<1.00 THEN ΔV_w = 0.33 mm/s

R7: IF γ≥1.00 THEN ΔV_w = 0.50 mm/s

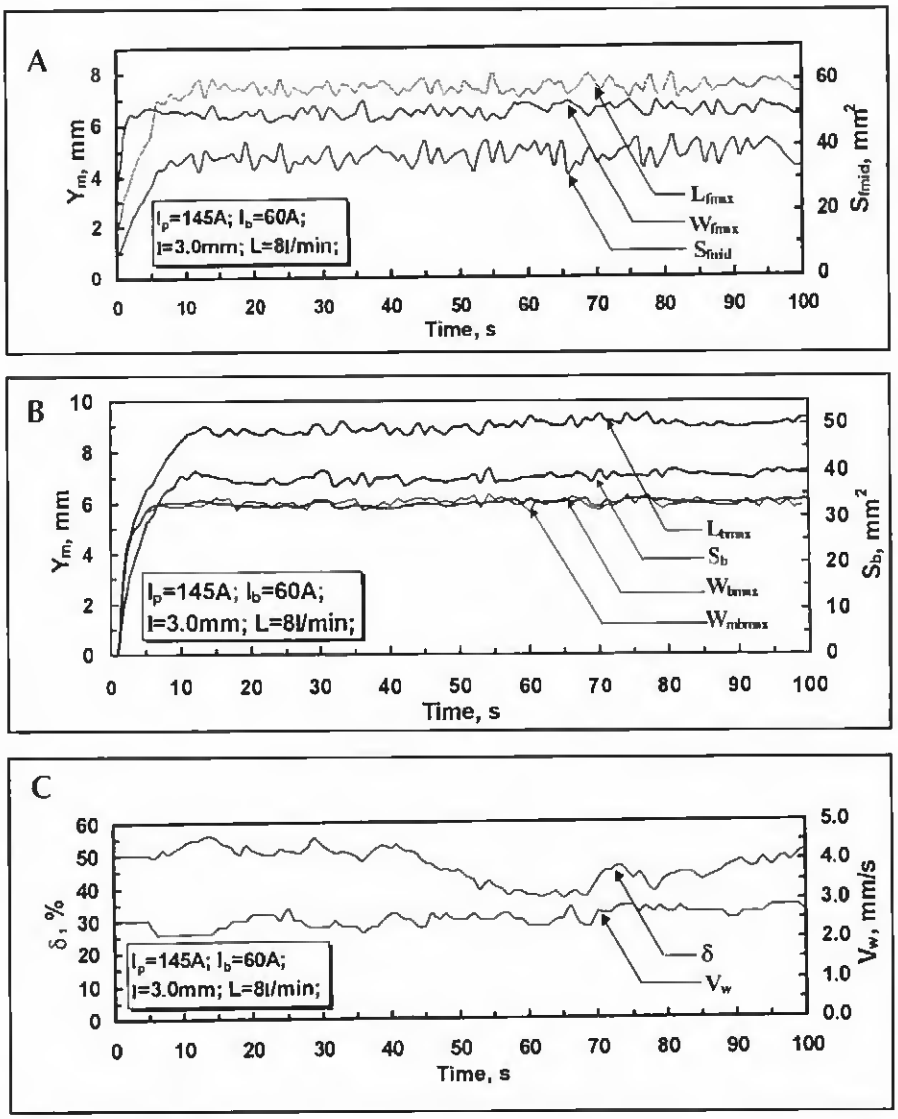

Fig. 15 — The double-input and double-output intelligent control curves of the dumbbell-shaped workpiece during pulsed gas tungsten arc welding. A — Topside sizes of the weld pool; B — backside sizes of the weld pool; C — control variables.

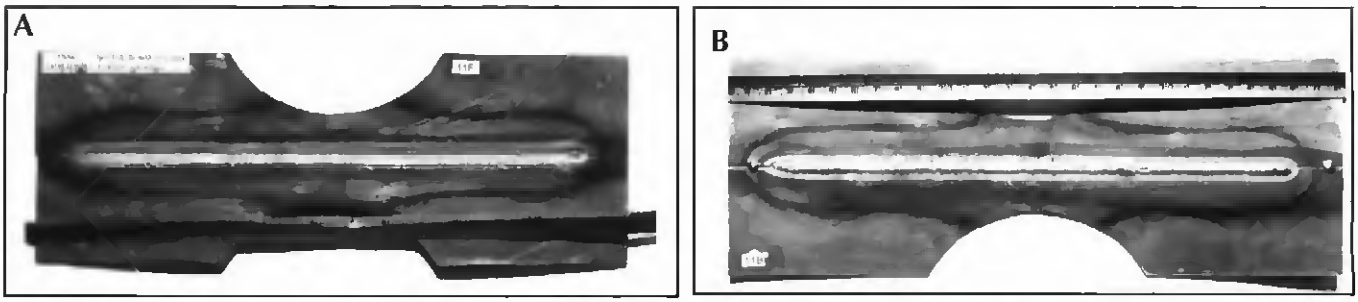

Fig. 16 — The dumbbell-shaped workpiece with the double-input and double-output intelligent controller. A — Topside; B — backside.

The Controlled Welding Experiments Using the DIDO Intelligent Controller

To verify the performance of the DIDO intelligent controller, welding experiments were conducted on dumbbell-shaped specimens. The minimum regulating unit of δ was 1% and the minimum regulating unit of V_w was 0.17 mm/s. Given W_{mbmax} was 6.0 mm, the control curve was derived as shown in Fig. 15, and the topside and backside are shown in Fig. 16. From the control results, the size parameters in both the width direction and the length direction are controlled perfectly. The geometry parameters are more stable than the results generated with the single variable controller. The results can be seen in the figures.

Statistical results showed the maximum error of W_{bmax} was 0.34 mm, the average error was 0.09 mm and the root-mean-square error was 0.11 mm. Other statistical results of L_{fmax}, S_{fmid}, L_{bmax} and S_b were smaller than that of the single variable controller. All the results testify to the feasibility and accuracy of the DIDO intelligent controller.

Conclusions

Intelligent techniques that incorporated computer vision, neural networks modeling, a self-learning fuzzy neural network controller, and a double-input and double-output intelligent controller were investigated and applied successfully to the pulsed gas tungsten arc welding of butt joints.

1) The shape parameters proposed in this paper along with the size parameters of the weld pool developed in a previous bead-on-plate welding investigation were combined to characterize the weld pool geometry. A new real-time algorithm was developed to determine the size and shape parameters.

2) The neural network model with both size and shape parameters as the inputs predicted the backside width more accurately than with single-size parameters as the model inputs.

3) The single-input and single-output fuzzy neural network controller was developed for controlling the backside width. Experiment results from butt joint welding a 2-mm-thick mild steel dumbbell-shaped specimen showed the backside width was successfully controlled.

4) A double-input and double-output intelligent controller incorporated with a single-variable fuzzy neural network controller and expert system was developed. The capability for controlling the geometry parameters in the length and width directions by regulating the pulse duty ratio and the travel speed was verified. A good weld shape was obtained with the double-input and double-output control system.

The intelligent methodology provided in this paper can be fully or partially implemented in other arc welding processes.

Acknowledgments

This work was supported by the National Natural Science Foundation of China No. 59575057 and No. 59635160. The authors would like to thank the editor and anonymous referees for their careful review and constructive comments on this article.

References

1. Chen, S. B., Lou, Y. J., Wu, L., and Zhao, D. B. 2000. Intelligent methodology for sensing, modeling and control of pulsed GTAW: part 1 — bead-on-plate welding. *Welding Journal* 79(6): 151-s to 163-s.

2. Nagarajan, S., Chin, B. A., and Chen, W. 1992. Control of the welding process using infrared sensors. *IEEE Transactions on Robotics and Automation* 8(1): 86–93.

3. Chen, W. and Chin, B. A. 1990. Monitoring joint penetration using infrared sensing techniques. *Welding Journal* 69(4): 181-s to 185-s.

4. Hoffman, T. 1991. Real-time imaging for process control. *Advanced Materials & Processes* (9): 37–43.

5. Agapakis, J. E., and Bolstad, J. 1991. Vision sensing and processing system for monitoring and control of welding and other high luminosity processes. *International Robots and Vision Automation Conference*, pp. 23–28.

6. Kovacevic, R., and Zhang, Y. M. 1997. Real-time image processing for monitoring of free weld pool surface. *ASME Journal of Manufacturing Science and Engineering* 119(2):161–169.

7. Richardson, R. W., and Gutow, D. A. 1984. Coaxial arc weld pool viewing for process monitoring and control. *Welding Journal* 63(3): 43–50.

8. Pietrzak, K. A., and Packer, S. M. 1994. Vision-based weld pool width control. *ASME Journal of Engineering for Industry* 116(1): 86–92.

9. Brzakovic, D., and Khani, D. T. 1991. Weld pool edge detection for automated control of welding. *IEEE Transactions on Robotics and Automation* 7(3): 397–403.

10. Hardt, D. E., Garlow, D. A., and Weinert, J. B. 1985. A model of full penetration arc welding for control system design. *ASME Journal of Dynamic Systems, Measurement, and Control* 107: 40–46.

11. Zhang, Y. M., Wu, L., Walcott, B., and Chen, D. H. 1993. Determining joint penetration in GTAW with vision sensing of weld face geometry. *Welding Journal* 72(10): 463-s to 469-s.

12. Kovacevic, R., Zhang, Y. M., and Li, L. 1996. Monitoring of weld penetration based on weld pool geometrical appearance. *Welding Journal* 75(10): 317-s to 328-s.

13. Willis, M. J., and Montague, G. A. 1992. Artificial neural network in process estimation and control. *Automatica* 28(6): 1181–1187.

14. Andersen, K., and Cook, G. E. 1990. Artificial neural networks applied to arc welding process modeling and control. *IEEE Transaction Industry Application* 26(9): 824–830.

15. Chen, S. B., Wu, L., Wang, Q. L., and Liu, Y. C. 1997. Self-learning fuzzy neural network and computer vision for control of pulsed GTAW. *Welding Journal* 76(5): 201-s to 209-s.